

# Altermagnetism-Induced Parity Anomaly in Weak Topological Insulators

Yu-Hao Wan<sup>1</sup> and Qing-Feng Sun<sup>1,2,\*</sup>

<sup>1</sup>*International Center for Quantum Materials, School of Physics, Peking University, Beijing 100871, China*

<sup>2</sup>*Hefei National Laboratory, Hefei 230088, China*

We demonstrate that introducing altermagnetism on the surface of a weak topological insulator (TI) results in the emergence of a single massless Dirac fermion, exhibiting a parity anomaly. To explore the transport properties induced by this parity anomaly, we propose an effective two-dimensional (2D) lattice model to describe the weak TI surface. This model captures both the energy spectrum and spin texture of the weak TI surface while reducing computational complexity. We show that the weak TI surface hosts a half-integer chiral edge current under the influence of altermagnetism. Additionally, in the presence of decoherence, the Hall conductance attains a half-quantized value. Layer-resolved calculations from a 3D slab model further confirm that surface altermagnetism drives the surface Hall conductance to transition to  $e^2/2h$ , aligning with calculation from the 2D effective lattice model. Our findings establish a link between altermagnetism and quantum anomalies, positioning weak TIs as a potential platform for investigating the parity anomaly without a net magnetic moment.

## I. INTRODUCTION

Parity anomaly is a concept from high-energy physics, where a two dimensional massless Dirac fermion with parity symmetry couples to a gauge field, inevitably generating a small mass term that breaks parity symmetry through a regularization process[1–3]. The realization of parity anomaly in condensed matter systems is a fundamental problem and has been the subject of extensive research[4–16]. To achieve parity anomaly in condensed matter, the system must host a single Dirac cone. As a consequence of the parity anomaly, a single Dirac cone results in several significant observable effects. For example, in electronic systems, the parity anomaly leads to a half quantized Hall effect, as predicted by the anomaly-induced Chern-Simons theory[3, 11, 17–19]. In Majorana systems, where a massless Majorana fermion couples to a gravitational field, the parity anomaly gives rise to a gravitational Chern-Simons term, resulting in a quarter quantized thermal Hall conductance[20–24].

The realization of parity anomaly in condensed matter systems was first proposed by Haldane [17], who suggested that by introducing a staggered magnetic flux and adjusting the on-site energy difference between the A and B sublattices in a honeycomb lattice, the system could achieve parity anomaly when one of the two valleys is fine-tuned to close while the other remains gapped. However, Haldane’s proposal is difficult to realize in real materials due to the challenges in precisely tuning the staggered magnetic flux. Nevertheless, it has been successfully implemented in artificial system such as photonic [25, 26] and acoustic system[27]. Another approach to realizing the parity anomaly in condensed matter systems is through the use of the surface states of three dimensional topological insulators (3D TIs)[28–30]. Recently, experiments involving semi-magnetic 3D TIs have achieved this, successfully realizing the parity anomaly [31]. In these experiments, a magnetic moment was introduced on one surface of a 3D TI, which opened a gap in the Dirac cone on that

surface, while leaving the Dirac cone on the opposite surface gapless. This experimental setup led to the observation of the half quantized Hall effect, a direct consequence of the parity anomaly in the system.

While the parity anomaly has been experimentally realized on the surface of strong 3D TIs, its realization in weak 3D TIs remains a significant challenge. This difficulty arises from the fundamental difference in their topological properties: strong TIs, with nontrivial  $\mathbb{Z}_2$  topology, host a single Dirac cone on their surfaces, whereas weak TIs exhibit an even number of Dirac cones due to their trivial bulk  $\mathbb{Z}_2$  topological invariant[29]. Introducing ferromagnetic ordering in a weak TI would gap out all surface Dirac cones simultaneously, preventing the system from hosting the single Dirac cone necessary for the realization of the parity anomaly. Therefore, achieving the parity anomaly in weak 3D TIs requires a different mechanism from that used in strong TIs.

Altermagnetic magnetism, a distinct type of magnetic ordering, is believed to exist in various materials and can induce momentum-dependent spin splitting without net macroscopic magnetization[32–34]. This unique property has made altermagnetism a topic of considerable research interest, both theoretically and experimentally, with studies exploring its connections to superconductivity [35–41], topological phenomena [42, 43], magnetic multipoles [43, 44], and anomalous Hall effect[45].

In this work, we propose that altermagnetism can be employed to achieve the parity anomaly in weak 3D TIs. By introducing altermagnetism in proximity to the surface of weak TIs, one of the two gapless Dirac cones can be gapped out, leaving a single Dirac cone on the surface, which allows for the realization of the parity anomaly. To investigate the surface transport properties induced by the parity anomaly, we constructed a 2D lattice model for the surface of the weak 3D TI by introducing an anisotropic Wilson mass term. This 2D model effectively captures the linear dispersion of the Dirac cones at the  $\Gamma$  and  $Y$  points on the weak 3D TI surface. Additionally, the spin texture distribution obtained from the 2D lattice model closely matches the spin texture observed on the surface of the weak TI. Calculations of the equilibrium current reveal that the presence of a single Dirac cone leads

\* Corresponding author: sunqf@pku.edu.cn.

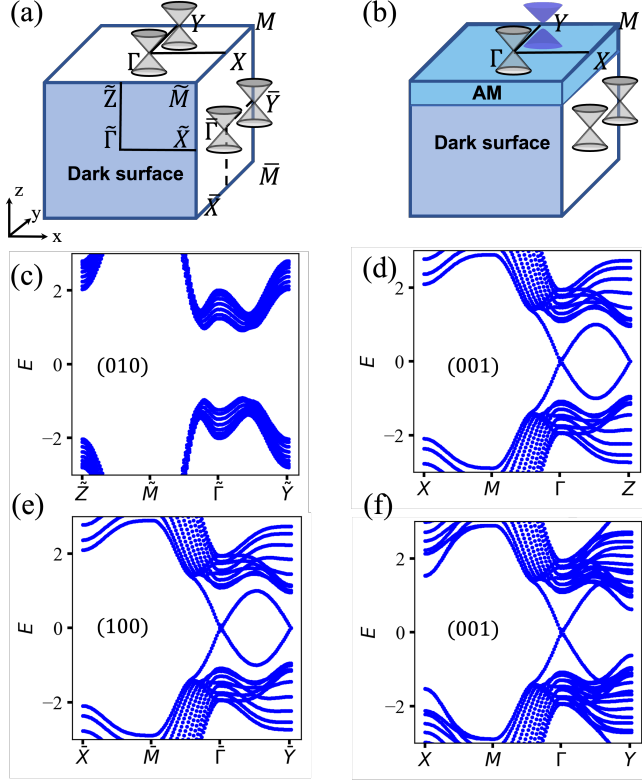


Figure 1. (a) Schematic of the weak TI, with the dark surface (010) marked in blue. Two gapless Dirac cones are present on the (100) and (001) surfaces. (b) On the (001) surface with altermagnetism, the Dirac cone at the  $Y$  point is gapped. (c-e) Band structures of the slab models stacked along the (010), (001), and (100) directions, respectively, without altermagnetism. (f) Energy spectrum of the slab model stacked along the (001) direction with altermagnetism applied on the surface, with an altermagnetic strength of  $J = 0.5$ .

to a half-integer chiral edge current. Furthermore, using the nonequilibrium Green's function method, we computed the Hall conductance under dephasing. The results show that, under dephasing, the half-quantized Hall conductance appears. Despite the absence of a net magnetic moment, the system still exhibits half quantized Hall conductance due to the parity anomaly. This finding establishes a profound connection between altermagnetism and quantum anomaly and offers a novel platform for studying the parity anomaly.

The rest of the paper is organized as follows. In Sec. II, we introduce the model Hamiltonian of the weak 3D TI and explain how a single Dirac cone is realized by introducing altermagnetism on the surface. In Sec. III, we present the 2D lattice model for the surface states of the weak 3D TI and validate its accuracy by comparing the band structure and spin texture with those of the weak 3D TI. In Sec. IV, using the 2D lattice model developed in Sec. III and considering the proximity of altermagnetism, we calculate the equilibrium current and the Hall conductance under dephasing. In Sec. V, we compute the layer-resolved Hall conductance distribution of the weak TI in the presence of surface-proximal altermagnetism. Finally, a brief summary is provided in Sec. VI.

## II. MODE HAMILTONIAN OF WEAK TI

We begin with the tight-binding Hamiltonian for the 3D TI in a cubic lattice[46]:

$$\mathcal{H} = \left( m - \sum_i 2B_i \right) s_0 \sigma_z + \sum_i (2B_i s_0 \sigma_z \cos k_i + A s_i \sigma_x \sin k_i), \quad (1)$$

where  $m$ ,  $B_i$ , and  $A$  are the model parameters, and  $k_i$  is the momentum with  $i = x, y, z$ . Here,  $s_i$  and  $\sigma_i$  are the Pauli matrices in the spin and orbital spaces, respectively. To position the system in the weak topological phase, we set  $A = 1$ ,  $B_y = 0.2$ ,  $B_x = B_z = 1$ , and  $m = 2$ , unless otherwise specified. Under these parameters, the system has a  $\mathbb{Z}_4$  index of  $(0, 010)$ [29, 47]. This  $\mathbb{Z}_4$  index signifies that the phase is adiabatically connected to QSH states stacked along the (010) direction, indicating the presence of an even number of Dirac cones on the (100) and (001) surfaces, while the (010) surface remains a gapped dark surface (See Fig. 1(a)). This behavior is similar to that of the realistic weak TI  $\text{ZrTe}_5$ [48], which features even Dirac cones on the side surfaces.

To investigate the surface energy spectrum, we construct 10-layers slab models stacked along  $l$ -directions. The Hamiltonian is represented as follows:

$$H_{\text{slab}}^l = \begin{pmatrix} H_{\text{lay}_1} & D & 0 & 0 \\ D^\dagger & H_{\text{lay}_2} & D & 0 \\ 0 & D^\dagger & \dots & D \\ 0 & 0 & D^\dagger & H_{\text{lay}_{10}} \end{pmatrix} \quad (2)$$

where  $l$  represents the stacking direction, which can be one of  $x, y, z$ . The Hamiltonian for each layer is given by:

$$H_{\text{lay}}(k_m, k_n) = A \sigma_x s_m \sin k_m + A \sigma_x s_n \sin k_n + [m + 2B_m(\cos k_m - 1) + 2B_n(\cos k_n - 1)] \sigma_z s_0,$$

where  $k_m$  and  $k_n$  represent the lattice momenta in the  $m$  and  $n$  directions, respectively, which are perpendicular to  $l$ . The interlayer hopping is given by:  $D = \frac{A}{2i} \sigma_x s_l + B_l \sigma_z s_0$ .

In Figures 1(c-e), we present the band spectrum derived from the slab models. The band spectrum for the slab model stacked along the (100) direction is gapped, indicating a "dark surface" in that direction. In contrast, the band spectra for the slab models stacked along the (001) and (010) directions exhibit two gapless Dirac cones located at the  $\Gamma/\bar{\Gamma}$  and  $Y/\bar{Y}$  points.

Subsequently, we introduce altermagnet coupled on the (001) surface to open the gap for the Dirac cones located at the  $Y$ , as depicted in Fig. 1(b). The proximity of the altermagnet modifies the surface Hamiltonian through the following term:

$$H_{\text{AM}}(k_x, k_y) = J(\cos k_x - \cos k_y) \sigma_0 s_z (\delta_{l,1} + \delta_{l,10}), \quad (3)$$

with  $J$  the altermagnetic strength. To facilitate the examination of the influence of surface altermagnetism on the energy band structure, symmetric magnetization is applied on both

the top and bottom surfaces. Figure 1(f) illustrates the band structure of the slab model stacked along the (001) direction after the introduction of the altermagnetic term. It is evident that the Dirac cone at the  $Y$  point becomes gapped, whereas the Dirac cone at the  $\Gamma$  point remains gapless. This suggests that altermagnet can give rise to a surface with a single gapless Dirac cone in a weak TI.

### III. THE 2D LATTICE MODEL FOR THE SURFACE STATES OF THE WEAK 3D TI

To study the transport properties of the surface states, directly computing based on the Hamiltonian derived from a 3D lattice model can be computationally expensive. Achieving high-precision results often requires working with an extremely large Hilbert space. Although weak 3D TIs exhibit an insulating bulk state, their surface states near the Dirac nodes can be effectively described by a massless 2D Dirac Hamiltonian at low energies. Compared to 3D lattice models, 2D lattice models significantly reduce computational complexity while preserving key physical properties. In the case of strong 3D TIs, well-established 2D lattice models already exist[49]. However, for weak 3D TIs, there is still a lack of an efficient lattice model to describe their surface states.

Next, we construct a 2D lattice model for the surface of a weak TI, specifically considering the (001) surface. We start from a Hamiltonian of massless 2D Dirac fermion:  $H_{Dirac} = \tilde{A}(k_x\sigma_x + k_y\sigma_y)$ , where  $\tilde{A}$  is a parameter corresponding to the Dirac fermion velocity. We discretize it on a square lattice by replacing  $k_i \rightarrow \frac{1}{a}\sin(k_i a)$ , where  $a$  is the lattice constant, and we set  $a = 1$  for simplicity. Thus, the lattice Hamiltonian of the 2D Dirac fermion becomes:

$$H_{Dirac}^{Lattice} = \tilde{A}[\sin(k_x)s_x + \sin(k_y)s_y]. \quad (4)$$

Due to the fermion doubling problem in lattice models of massless Dirac fermions[1], there are Dirac cones at all four high-symmetry points  $\Gamma$ ,  $M$ ,  $X$ , and  $Y$ . However, for the surface of a weak 3D TI described by Eq.(1), we expect only two Dirac cones located at the  $\Gamma$  and  $Y$  points. To address this, we introduce an anisotropic Wilson mass term:

$$H_W^{aniso}(k_x, k_y) = 2\tilde{B}_x(1 - \cos(k_x))s_z. \quad (5)$$

Thus, the 2D lattice model for the surface of the weak 3D TI can be written as:

$$H_{surf} = H_{Dirac}^{Lattice} + H_W^{aniso}. \quad (6)$$

The anisotropic Wilson term vanishes as  $k_x$  approaches zero in a quadratic manner, which opens gaps at the Dirac cones at the  $M$  and  $X$  points while leaving the Dirac cones at the  $\Gamma$  and  $Y$  points gapless. This can be easily understood from the energy spectrum. The energy spectrum of  $H_{surf}$  can be expressed as:

$$E_{k_x, k_y}^2 = \tilde{A}^2 \sum_{i=x,y} \sin^2(k_i) + (4\tilde{B}_x)^2 \sin^4(k_x/2).$$

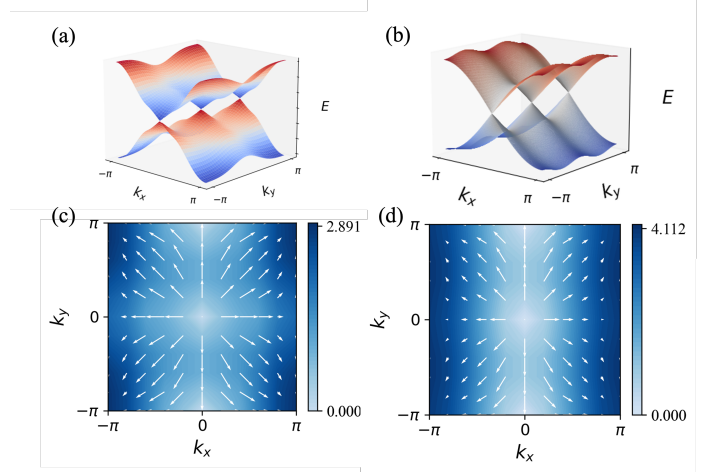


Figure 2. (a) Energy spectrum of the (001) surface of the weak 3D TI. (b) Energy spectrum of the 2D lattice model with  $\tilde{A} = 1$  and  $\tilde{B}_x = 1$ . (c, d) Spin textures of the positive-energy bands from (a) and (b), respectively, where the color represents the magnitude of the energy.

As  $(k_x, k_y) \rightarrow \Gamma$  or  $Y$ ,  $E^2$  approaches  $\tilde{A}^2 \sum_{i=x,y} q_i^2 + \tilde{B}_x^2 q_x^4$ , where  $q_x$  and  $q_y$  represent small deviations from the momenta near the  $\Gamma$  and  $Y$  points. This implies that the spectrum remains linearly dispersive at the  $\Gamma$  and  $Y$  points. However, as  $(k_x, k_y) \rightarrow X$  or  $M$ ,  $E^2$  approaches  $\tilde{A}^2 \sum_{i=x,y} q_i^2 + 16\tilde{B}_x^2$ , with the Wilson term opening a gap of size  $8\tilde{B}_x$  at the  $M$  and  $X$  points.

To demonstrate the 2D lattice model in Eq.(6) effectively captures the properties of the weak TI surface, we compare the surface spectrum of a weak 3D TI and the spectrum given by the 2D lattice model. Figures 2(a) and 2(b) show the band spectra of the (001) surface of the weak 3D TI and the band structure of 2D lattice model, respectively. In both cases, we observe two gapless Dirac cones at the  $\Gamma$  and  $Y$  points.

Furthermore, we compare the spin textures of the two models. Figure 2(c) shows the spin expectation value  $\langle \hat{\mathbf{S}} \rangle$  for the surface states of the weak 3D TI in the Brillouin zone, where  $\langle \hat{\mathbf{S}} \rangle = \sum_{i=x,y} \langle \psi_k | s_i \sigma_x | \psi_k \rangle$ , with  $|\psi_k\rangle$  representing the Bloch states of the surface states with positive energy at momentum  $k$ . From the spin texture, it is evident that the Dirac cones at the  $\Gamma$  and  $Y$  points exhibit opposite chirality, corresponding to Berry phases of  $+\pi$  and  $-\pi$ , respectively. Similarly, Figure 2(d) displays the spin texture obtained from the 2D lattice model. The spin texture derived from the lattice model closely resembles that of the weak 3D TI, particularly near the  $\Gamma$  and  $Y$  points, reflecting the same chirality as observed in the 3D model's calculations.

In constructing the effective surface model for weak TIs, the introduction of an anisotropic Wilson mass term effectively captures the underlying physics. A weak TI with a  $\mathbb{Z}_4$  index of (0,010) can be viewed as a stack of quantum spin Hall (QSH) states along the (010) direction[29, 47], where the surface states can be considered as being composed of

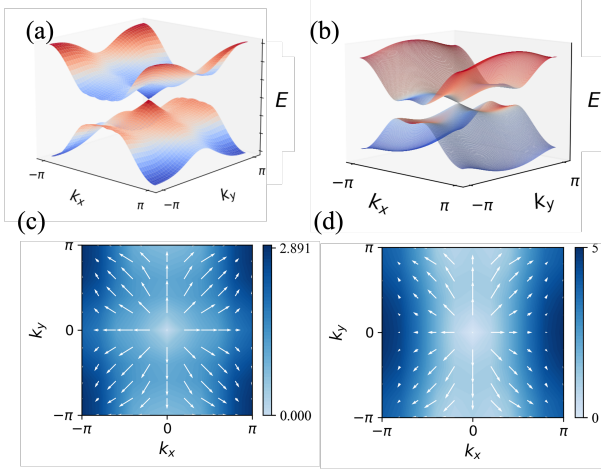


Figure 3. (a) Energy spectrum of the (001) surface of the weak 3D TI under altermagnetism, with  $J = 0.5$ . (b) Energy spectrum of the 2D lattice model under altermagnetism, with  $\tilde{A} = 1$ ,  $\tilde{B}_x = 1$ , and  $J = 0.5$ . (c, d) Spin textures of the positive-energy bands from (a) and (b), respectively, where the color represents the magnitude of the energy.

quasi-one-dimensional edge states derived from the QSH layers. Consequently, the origin of the surface states in weak TIs can be attributed to the topological properties of the stacked QSH layers. Therefore, when constructing the lattice Hamiltonian for the surface, we introduce a Wilson mass term along the in-plane direction of the QSH layers to capture the influence of the nontrivial bulk topology of the QSH states on the boundaries.

Next, we introduce altermagnetic term,  $J(\cos k_x - \cos k_y)s_z$ , to 2D lattice model. Under the influence of altermagnetism, the energy spectrum becomes  $E_{k_x, k_y}^2 = \tilde{A}^2 \sum_{i=x, y} \sin^2(k_i) + [(4\tilde{B}_x) \sin^2(k_x/2) + J(\cos k_x - \cos k_y)]^2$ . In this case, as  $(k_x, k_y) \rightarrow Y$ ,  $E^2$  approaches  $\tilde{A}^2 \sum_{i=x, y} q_i^2 + 4J^2$ . The Dirac cone at the  $Y$  point is gapped due to the introduction of altermagnetism, resulting in a gap of  $4J$ , while leaving only a single gapless Dirac cone at the  $\Gamma$  point. Figures 3(a) and (b) display the energy spectra for the weak TI surface and the 2D lattice model under the influence of altermagnetism, both showing a gapless Dirac cone at the  $\Gamma$  point. Furthermore, the introduction of altermagnetism does not affect the distribution of the spin texture. Figures 3(c) and (d) illustrate the spin textures for the weak TI surface and the 2D lattice model, respectively. In both cases, a clockwise winding spin texture is observed around the  $\Gamma$  point, corresponding to a Berry phase of  $\pi$ .

#### IV. EQUILIBRIUM FLOW AND HALF-QUANTIZED HALL CONDUCTANCE

Building on the 2D lattice model for the surface of the weak 3D TI, we now proceed to investigate the transport properties of the surface under the influence of altermagnetism. This

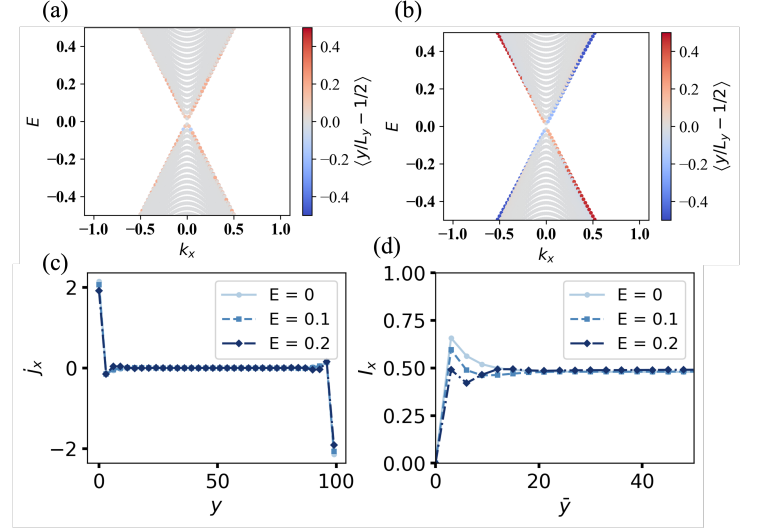


Figure 4. (a, b) Band structure of the nanoribbon, with colors indicating the average displacement relative to the center for each Bloch state,  $\langle y/L_y - 1/2 \rangle$ . The calculation is performed with  $L_y = 100$ , and for  $J = 0$  in (a) and  $J = 0.5$  in (b). (c) Distribution of the equilibrium current along the  $y$ -direction at different energies. (d) Variation of the current flux as the summation range  $\bar{y}$  increases.

approach allows us to focus specifically on the surface states' behavior while also significantly reducing the computational complexity compared to a full 3D model. To begin, we derive the Hamiltonian for the nanoribbon by discretizing  $H_{surf}$  in Eq.(6) along the  $y$ -direction while maintaining translational symmetry in the  $x$ -direction:

$$H_{quasi-1D} = \sum_{k_x, y} \left( c_{k_x, y}^\dagger T_y c_{k_x, y+1} + \text{h.c.} \right) + c_{k_x, y}^\dagger \left[ \tilde{A} \sin(k_x) s_x + 2\tilde{B}_x (1 - \cos(k_x)) s_z + J \cos k_x s_z \right] c_{k_x, y} \quad (7)$$

where  $c_{k_x, y}^\dagger$  and  $c_{k_x, y}$  are creation and annihilation operators at position  $y$  with momentum  $k_x$  and  $T_y = -i\tilde{A}s_y - \frac{J}{2}s_z$ .

Figures 4(a) and 4(b) show the energy spectrum of the single gapless Dirac cone at the  $\Gamma$  point for a nanoribbon along the  $x$ -direction with  $J = 0$  and  $J = 0.5$ , respectively. The color in the plots represents the average displacement relative to the center for each Bloch state,  $\langle y/L_y - 1/2 \rangle$  with  $L_y$  the width of the nanoribbon. Without altermagnetism ( $J = 0$ ), the energy spectrum does not reveal any obvious chiral features [see Fig. 4(a)]. However, after introducing altermagnetism ( $J = 0.5$ ), the states on the left and right sides of the energy spectrum with opposite velocities locate at the upper and lower sides of the nanoribbon (exhibiting the red and blue colors in Fig. 4(b)), respectively, indicating the emergence of chirality. This behavior reflects the breaking of time-reversal symmetry at the surface due to altermagnetic effects, leading to the separation of counterpropagating modes. Despite lacking a net magnetic moment, altermagnetism can still induce and control chiral edge states.



To further illustrate the altermagnetism-induced chiral nature on the surface of the weak 3D TI, we further calculated the equilibrium current distribution for the case of  $J = 0.5$ , with the equilibrium current  $j_x$  denoted as[50]:

$$j_x(E, y) = -\frac{e}{\pi h} \int_{-\pi}^{\pi} \text{Im Tr} \left[ \frac{\partial H(k_x)}{\partial k_x} G_{k_x}^R(E, y, y) \right] dk_y,$$

where  $G_{k_y}^R(E, y, y')$  is the retarded Green's function for  $H(k_x)$ , written as  $G_{k_x}^R(E, y, y') = \langle y | (E - H(k_x) + i\eta)^{-1} | y' \rangle$ , with  $\eta = 0.1$ . Fig. 4(c) shows the distribution of the equilibrium current  $j_x$  in the  $y$ -direction for different energies. The existence of counterpropagating currents at the upper and lower boundaries confirms the chiral nature of the system. Furthermore, as shown in Fig. 4(d), the current flux at different energies,  $I_x(E, \bar{y}) = \int_0^{\bar{y}} dy j_x(E, y)$  ( $\bar{y} < L_y/2$ ) gradually converges to  $1/2$  as  $\bar{y}$  increases, demonstrating the presence of the half quantized equilibrium current, a hallmark of systems exhibiting parity anomaly[51].

In fact, this half-integer equilibrium current is related to the half quantized Hall conductance of the system. Experimentally, the Hall conductance can be measured using a six-terminal transport Hall-bar setup. For numerical simulations, we proceed by discretizing Hamiltonian  $H$  in both the  $x$ - and  $y$ -directions, with the lengths  $L_x$  and  $L_y$  both set to 180 in the following calculations. We then construct a six-terminal Hall-bar device (see Fig. 5(a)), where terminals I and IV are current leads, and terminals II, III, V, and VI serve as voltage probes. The dephasing effect is simulated by introducing Buttiker virtual leads between each pair of lattice sites[52–54], represented by the red spheres in Fig. 5(a).

Using the Landauer-Büttiker formula, the current at terminal  $n$  at zero temperature is given by[55–57]:

$$I_n = \sum_{m \neq n} \frac{e^2}{h} (T_{mn} V_n - T_{nm} V_m), \quad (8)$$

where  $V_m$  is the voltage at lead  $m$ , and  $T_{nm}(E_F)$  denotes the transmission coefficient at energy  $E_F$  from lead  $m$  to lead  $n$ . The transmission coefficient is expressed as:  $T_{nm}(E) = \text{Tr}[\Gamma_n \mathbf{G}^R \Gamma_m \mathbf{G}^A]$ , where  $\Gamma_{m/n} = i(\Sigma_{m/n}^r - \Sigma_{m/n}^a)$  is the line-width function for leads  $m/n$ , with  $\Sigma_{m/n}^r$  and  $\Sigma_{m/n}^a$  being the retarded and advanced self-energies due to the coupling of the leads  $m/n$ , respectively. The retarded Green's function  $\mathbf{G}^R(E)$  is given by:  $\mathbf{G}^R(E) = [\mathbf{G}^A]^\dagger = [(E + i\eta)\mathbf{I} - \mathbf{H} - \sum_n \Sigma_n^r]^{-1}$ . For the virtual leads, the self-energy is  $\Sigma_n^r = -\frac{i}{2}\Gamma_v I_n$ , where  $\Gamma_v$  is the dephasing strength [53], and  $I_n$  is a  $2 \times 2$  identity matrix. Using Eq. (8) and assuming the voltage of the left (I) and right (IV) terminals being  $V/2$  and  $-V/2$ , we can calculate the currents and voltages at all terminals. Due to current conservation, we have  $|I_1| = |I_4|$ , and the Hall resistance  $R_{xy}$  and longitudinal resistance  $R_{xx}$  are obtained as:

$$R_{xy} = \frac{V_2 - V_6}{I_2}, \quad R_{xx} = \frac{V_2 - V_3}{I_2}. \quad (9)$$

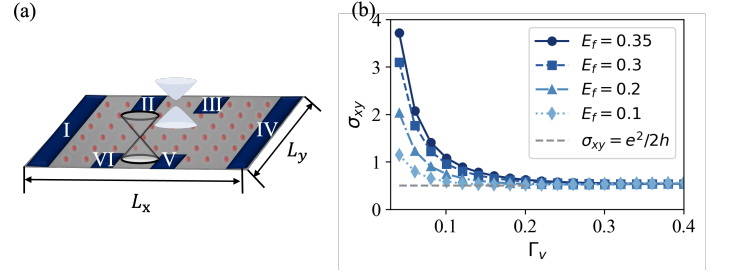


Figure 5. (a) Illustration of the 2D lattice model of the surface of a weak 3D TI, with the attached ports shown in dark blue. Due to the effect of altermagnetism, only a single gapless Dirac cone exists on the surface. The red balls represent the virtual leads. (b) Hall conductance as a function of dephasing strength  $\Gamma_v$  for different Fermi energy levels  $E_F$ .

The resistivities are given by  $\rho_{xy} = R_{xy}$  and  $\rho_{xx} = \frac{R_{xx}}{l_1/L_y}$ , where  $l_1$  is the distance between leads II and III, set to 10 in the calculations. Finally, the Hall conductance is determined by:

$$\sigma_{xy} = \frac{\rho_{xy}}{\rho_{xy}^2 + \rho_{xx}^2}. \quad (10)$$

Figure 5(b) shows the variation of the calculated Hall conductance as the dephasing strength  $\Gamma_v$  increases at different Fermi energy levels. As the dephasing strength increases, the Hall conductance rapidly decays to  $e^2/2h$ . This half-quantized Hall conductance is independent of the Fermi energy, a characteristic consistent with the parity anomaly observed in semi-magnetic TIs[11, 31]. It is important to consider the dephasing effect because, in real experiments, sample sizes often extend to several hundred micrometers, far exceeding the decoherence length, thus necessitating the inclusion of dephasing in the analysis.

## V. LAYER-RESOLVED HALL CONDUCTANCE

After discussing the transport properties derived from the 2D lattice model for the surface of the weak 3D TI, we now turn our attention to the layer-resolved Hall conductance in a weak 3D TI[58–60]. This layer-resolved Hall conductance can be obtained by calculating the local Chern number, where the Hall conductance in layer  $l$  is related to the local Chern number between layers through the relation  $\sigma_{xy}(l) = C_z(l) \frac{e^2}{h}$ , with  $C_z(l)$  representing the local Chern marker along the  $z$ -direction.

We add an altermagnetic term  $J(\cos k_x - \cos k_y)\sigma_0 \otimes s_z \delta_{l,1}$  to the first layer of the 10-layer slab model in Eq. (2). Afterward, we compute the local Chern marker projected onto layer  $l$ , denoted as  $C_z(l)$ . The expression for the local Chern marker is given by [58]:

$$C_z(l) = \frac{-4\pi}{\mathcal{A}} \text{Im} \frac{1}{N_k} \sum_k \sum_{v,v',c} X_{vck} Y_{v'ck}^\dagger \rho_{vv'k}(l), \quad (11)$$

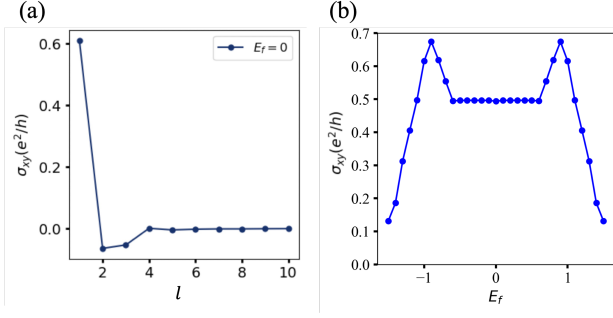


Figure 6. (a) Layer-resolved Hall conductance  $\sigma_{xy}(l)$  as a function of the layer index  $l$ . (b) Surface Hall conductance  $\sigma_{xy}^{\text{surf}}$  as a function of the Fermi energy  $E_f$ .

where  $\mathcal{A}$  represents the unit cell area,  $N_k$  is the number of  $k$ -points, and  $\rho_{vv'k}(l)$  is the projection matrix onto the orbitals within layer  $l$ , summing over all orbitals belonging to that layer.  $X$  and  $Y$  denote the position operators along the  $x$ - and  $y$ -directions, respectively. The matrix elements of the position operator, denoted as:

$$X(Y)_{vck} = \langle \psi_{v\mathbf{k}} | x(y) | \psi_{c\mathbf{k}} \rangle = \frac{\langle \psi_{v\mathbf{k}} | i\hbar v_x(v_y) | \psi_{c\mathbf{k}} \rangle}{E_{c\mathbf{k}} - E_{v\mathbf{k}}}, \quad (12)$$

are related to the energy difference between the conduction and valence bands,  $E_{c\mathbf{k}} - E_{v\mathbf{k}}$ , where  $v$  and  $c$  refer to the valence and conduction bands, respectively.

Figure 6(a) illustrates the layer-resolved Hall conductance distribution at  $E_f = 0$ . Due to the introduction of altermagnetism at  $l = 1$ , which breaks time-reversal symmetry, the Hall conductance becomes non-zero in the first three layers, while the local anomalous Hall conductance (AHC) becomes nearly zero for  $l > 3$ . It is important to note that the layer-resolved Hall conductance distribution is largely independent of the Fermi level, which is why we focus on the case of  $E_f = 0$  for clarity. The surface Chern number is determined by summing the local Chern markers from the first few layers [58, 61]. Therefore, we define the surface AHC as  $\sigma_{xy}^{\text{surf}} = \sum_{l=1}^3 \sigma_{xy}(l)$ . Under this definition, Fig. 6(a) shows that the surface Hall conductance at  $E_f = 0$  approaches  $e^2/2h$ .

Figure 6(b) presents the variation of the surface AHC  $\sigma_{xy}^{\text{surf}}$  with the Fermi level, revealing a plateau at  $e^2/2h$  in the central energy region. This plateau occurs where the Fermi level intersects only a single Dirac cone, signifying the persistence of the half-quantized Hall conductance across a range of energies. The origin of this Fermi level-independent half-quantization lies in the parity invariance of the Fermi surface, ensuring the robustness of the topological behavior induced by altermagnetism, even as the Fermi level varies [62].

## VI. DISCUSSION AND CONCLUSION

Before concluding, we will discuss the differences between realizing the parity anomaly in weak 3D TIs and in strong

3D TIs. Although lattice regularization is absent in strong 3D TIs, field theories with anomalies can describe the boundary states of topological phases in a higher spatial dimension. This explains why 2+1D massless Dirac fermions with parity anomaly can exist on the surface of a strong 3D TI [29]. The topological surface states avoid violating the fermion doubling theorem because their ultraviolet completion resides in the bulk. This manifests in the behavior of surface states on the top and bottom surfaces of a strong 3D TI, where at higher momentum, the surface states gradually evolve into bulk states. This evolution enables coupling between the top and bottom surface states at high momentum [62, 63]. Consequently, in the case of a semi-magnetic TI, when time-reversal symmetry is broken on one surface, the other surface can still support a massless linear dispersion at low energies, while incorporating a term that breaks time-reversal symmetry at higher energy, leading to the emergence of half quantized Hall conductance [62].

For weak 3D TIs, the strong  $\mathbb{Z}_2$  invariant is equal to 0, leading to a fermion doubling problem on the surface. Due to lattice regularization, a gapless Dirac cone with chirality opposite to that at the  $\Gamma$  point emerges at the  $Y$  point. This makes it impossible to realize a parity anomaly through conventional mechanisms used in 3D TIs, such as introducing ferromagnetism on one surface.

In this work, we demonstrate that the introduction of altermagnetism allows weak topological insulators to achieve the realization of the parity anomaly. It preserves time-reversal symmetry at low energies near the  $\Gamma$  point while breaking it at the  $Y$  point, where the gapless Dirac cone present can be understood as a result of lattice regularization. Here, altermagnetism replaces the role of lattice regularization, thereby avoiding the fermion doubling problem. This enables the surface to support a single gapless Dirac cone, resulting in a half-quantized Hall conductance due to the parity anomaly.

Our model can be regarded as an experimentally feasible adaptation of the Haldane model. Like the Haldane model, our approach does not require a net magnetic field to realize the parity anomaly. However, unlike the Haldane model, which demands fine-tuning and relies on staggered magnetic fluxes that are challenging to achieve experimentally, our approach involves introducing altermagnetism on the surface of a weak TI, which can be achieved experimentally through proximity effects and is significantly easier to implement.

The combination of altermagnetism and weak TIs is particularly promising because both types of materials have already been explored experimentally. Altermagnetism has been observed in materials such as MnTe [32, 64], CrSb [65], RuO<sub>2</sub> [66], while several materials, including Bi<sub>4</sub>I<sub>4</sub> [67], ZrTe<sub>5</sub> [48], Bi<sub>4</sub>Br<sub>2</sub>I<sub>2</sub> [68], have been experimentally confirmed as weak TIs. Notably, a recent experiment has demonstrated the stability of surface states in weak topological insulators [69]. Given the experimental verification of these key ingredients, we believe that the approach presented in this paper is experimentally feasible.

## ACKNOWLEDGEMENTS

Y.-H. W. is grateful to L.-D. Z. for fruitful discussions. This work was financially supported by NSF-China (Grants No. 11921005 and No. 12374034), the Innovation Program for

Quantum Science and Technology (No. 2021ZD0302403), and the Strategic priority Research Program of the Chinese Academy of Sciences (Grant No. XDB28000000). We also acknowledge the High-performance Computing Platform of Peking University for providing computational resources.

- 
- [1] A. N. Redlich, Gauge Noninvariance and Parity Nonconservation of Three-Dimensional Fermions, *Phys. Rev. Lett.* **52**, 18 (1984).
  - [2] A. N. Redlich, Parity violation and gauge noninvariance of the effective gauge field action in three dimensions, *Phys. Rev. D* **29**, 2366 (1984).
  - [3] G. W. Semenoff, Condensed-Matter Simulation of a Three-Dimensional Anomaly, *Phys. Rev. Lett.* **53**, 2449 (1984).
  - [4] J. Böttcher, C. Tutschku, L. W. Molenkamp, and E. M. Hankiewicz, Survival of the Quantum Anomalous Hall Effect in Orbital Magnetic Fields as a Consequence of the Parity Anomaly, *Phys. Rev. Lett.* **123**, 226602 (2019).
  - [5] C.-Z. Chang, J. Zhang, X. Feng, J. Shen, Z. Zhang, M. Guo, K. Li, Y. Ou, P. Wei, L.-L. Wang, Z.-Q. Ji, Y. Feng, S. Ji, X. Chen, J. Jia, X. Dai, Z. Fang, S.-C. Zhang, K. He, Y. Wang, L. Lu, X.-C. Ma, and Q.-K. Xue, Experimental Observation of the Quantum Anomalous Hall Effect in a Magnetic Topological Insulator, *Science* **340**, 167 (2013).
  - [6] S. Zhang, L. Pi, R. Wang, G. Yu, X.-C. Pan, Z. Wei, J. Zhang, C. Xi, Z. Bai, F. Fei, M. Wang, J. Liao, Y. Li, X. Wang, F. Song, Y. Zhang, B. Wang, D. Xing, and G. Wang, Anomalous quantization trajectory and parity anomaly in Co cluster decorated BiSbTeSe<sub>2</sub> nanodevices, *Nat. Commun.* **8**, 977 (2017).
  - [7] J. W. McIver, B. Schulte, F.-U. Stein, T. Matsuyama, G. Jotzu, G. Meier, and A. Cavalleri, Light-induced anomalous Hall effect in graphene, *Nat. Phys.* **16**, 38 (2020).
  - [8] L. Lu, Topology on a breadboard, *Nat. Phys.* **14**, 875 (2018).
  - [9] T. Ozawa, H. M. Price, A. Amo, N. Goldman, M. Hafezi, L. Lu, M. C. Rechtsman, D. Schuster, J. Simon, O. Zilberberg, and I. Carusotto, Topological photonics, *Rev. Mod. Phys.* **91**, 015006 (2019).
  - [10] G. Jotzu, M. Messer, R. Desbuquois, M. Lebrat, T. Uehlinger, D. Greif, and T. Esslinger, Experimental realization of the topological Haldane model with ultracold fermions, *Nature* **515**, 237 (2014).
  - [11] H. Zhou, H. Li, D.-H. Xu, C.-Z. Chen, Q.-F. Sun, and X. C. Xie, Transport Theory of Half-Quantized Hall Conductance in a Semimagnetic Topological Insulator, *Phys. Rev. Lett.* **129**, 096601 (2022).
  - [12] Y. Xu, I. Miotkowski, C. Liu, J. Tian, H. Nam, N. Alidoust, J. Hu, C.-K. Shih, M. Z. Hasan, and Y. P. Chen, Observation of topological surface state quantum Hall effect in an intrinsic three-dimensional topological insulator, *Nat. Phys.* **10**, 956 (2014).
  - [13] Y. Tokura, K. Yasuda, and A. Tsukazaki, Magnetic topological insulators, *Nat. Rev. Phys.* **1**, 126 (2019).
  - [14] Z. Ning, X. Ding, D.-H. Xu, and R. Wang, Robustness of half-integer quantized Hall conductivity against disorder in an anisotropic Dirac semimetal with parity anomaly, *Phys. Rev. B* **108**, L041104 (2023).
  - [15] B.-J. Yang and N. Nagaosa, Classification of stable three-dimensional Dirac semimetals with nontrivial topology, *Nat. Commun.* **5**, 4898 (2014).
  - [16] B. Fu, J.-Y. Zou, Z.-A. Hu, H.-W. Wang, and S.-Q. Shen, Quantum anomalous semimetals, *npj Quantum Mater.* **7**, 1 (2022).
  - [17] F. D. M. Haldane, Model for a Quantum Hall Effect without Landau Levels: Condensed-Matter Realization of the "Parity Anomaly", *Phys. Rev. Lett.* **61**, 2015 (1988).
  - [18] M. F. Lapa, Parity anomaly from the Hamiltonian point of view, *Phys. Rev. B* **99**, 235144 (2019).
  - [19] A. A. Burkov, Dirac fermion duality and the parity anomaly, *Phys. Rev. B* **99**, 035124 (2019).
  - [20] A. Furusaki, N. Nagaosa, K. Nomura, S. Ryu, and T. Takayanagi, Electromagnetic and thermal responses in topological matter: Topological terms, quantum anomalies and D-branes, *Comptes Rendus Physique* **14**, 871 (2013,11).
  - [21] A. Sekine and K. Nomura, Axion electrodynamics in topological materials, *Journal of Applied Physics* **129**, 141101 (2021).
  - [22] M. Sato and S. Fujimoto, Majorana Fermions and Topology in Superconductors, *J. Phys. Soc. Jpn.* **85**, 072001 (2016).
  - [23] Z. Wang, X.-L. Qi, and S.-C. Zhang, Topological field theory and thermal responses of interacting topological superconductors, *Phys. Rev. B* **84**, 014527 (2011).
  - [24] Y.-H. Wan and Q.-F. Sun, Quarter-quantized thermal Hall effect with parity anomaly, *Phys. Rev. B* **109**, 195408 (2024).
  - [25] G.-G. Liu, P. Zhou, Y. Yang, H. Xue, X. Ren, X. Lin, H.-x. Sun, L. Bi, Y. Chong, and B. Zhang, Observation of an unpaired photonic Dirac point, *Nat. Commun.* **11**, 1873 (2020).
  - [26] J. Lu, C. Qiu, L. Ye, X. Fan, M. Ke, F. Zhang, and Z. Liu, Observation of topological valley transport of sound in sonic crystals, *Nat. Phys.* **13**, 369 (2017,4).
  - [27] Y. Ding, Y. Peng, Y. Zhu, X. Fan, J. Yang, B. Liang, X. Zhu, X. Wan, and J. Cheng, Experimental Demonstration of Acoustic Chern Insulators, *Phys. Rev. Lett.* **122**, 014302 (2019).
  - [28] X.-L. Qi, T. L. Hughes, and S.-C. Zhang, Topological field theory of time-reversal invariant insulators, *Phys. Rev. B* **78**, 195424 (2008).
  - [29] L. Fu, C. L. Kane, and E. J. Mele, Topological Insulators in Three Dimensions, *Phys. Rev. Lett.* **98**, 106803 (2007).
  - [30] X.-L. Qi and S.-C. Zhang, Topological insulators and superconductors, *Rev. Mod. Phys.* **83**, 1057 (2011).
  - [31] M. Mogi, Y. Okamura, M. Kawamura, R. Yoshimi, K. Yasuda, A. Tsukazaki, K. S. Takahashi, T. Morimoto, N. Nagaosa, M. Kawasaki, Y. Takahashi, and Y. Tokura, Experimental signature of the parity anomaly in a semi-magnetic topological insulator, *Nat. Phys.* **18**, 390 (2022).
  - [32] J. Krempaský, L. Šmejkal, S. W. D'Souza, M. Hajlaoui, G. Springholz, K. Uhlířová, F. Alarab, P. C. Constantinou, V. Strocov, D. Usanov, W. R. Pudelko, R. González-Hernández, A. Birk Hellenes, Z. Jansa, H. Reichlová, Z. Šobán, R. D. González Betancourt, P. Wadley, J. Sinova, D. Kriegner, J. Minár, J. H. Dil, and T. Jungwirth, Altermagnetic lifting of Kramers spin degeneracy, *Nature* **626**, 517 (2024).
  - [33] I. I. Mazin, K. Koepernik, M. D. Johannes, R. González-Hernández, and L. Šmejkal, Prediction of unconventional magnetism in doped FeSb<sub>2</sub>, *Proc. Natl. Acad. Sci. U.S.A.* **118**, e2108924118 (2021).

- [34] L. Šmejkal, J. Sinova, and T. Jungwirth, Beyond Conventional Ferromagnetism and Antiferromagnetism: A Phase with Non-relativistic Spin and Crystal Rotation Symmetry, *Phys. Rev. X* **12**, 031042 (2022).
- [35] L. Šmejkal, J. Sinova, and T. Jungwirth, Emerging Research Landscape of Altermagnetism, *Phys. Rev. X* **12**, 040501 (2022).
- [36] J. A. Ouassou, A. Brataas, and J. Linder, Dc Josephson Effect in Altermagnets, *Phys. Rev. Lett.* **131**, 076003 (2023).
- [37] D. Chakraborty and A. M. Black-Schaffer, Zero-field finite-momentum and field-induced superconductivity in altermagnets, *Phys. Rev. B* **110**, L060508 (2024).
- [38] Q. Cheng, Y. Mao, and Q.-F. Sun, Field-free Josephson diode effect in altermagnet/normal metal/altermagnet junctions, *Phys. Rev. B* **110**, 014518 (2024).
- [39] S. Banerjee and M. S. Scheurer, Altermagnetic superconducting diode effect, *Phys. Rev. B* **110**, 024503 (2024).
- [40] H. G. Giil and J. Linder, Superconductor-altermagnet memory functionality without stray fields, *Phys. Rev. B* **109**, 134511 (2024).
- [41] C. Sun, A. Brataas, and J. Linder, Andreev reflection in altermagnets, *Phys. Rev. B* **108**, 054511 (2023).
- [42] Y.-X. Li, Y. Liu, and C.-C. Liu, Creation and manipulation of higher-order topological states by altermagnets, *Phys. Rev. B* **109**, L201109 (2024).
- [43] R. M. Fernandes, V. S. de Carvalho, T. Birol, and R. G. Pereira, Topological transition from nodal to nodeless Zeeman splitting in altermagnets, *Phys. Rev. B* **109**, 024404 (2024).
- [44] S. Bhowal and N. A. Spaldin, Ferroically Ordered Magnetic Octupoles in d-Wave Altermagnets, *Phys. Rev. X* **14**, 10.1103/PhysRevX.14.011019 (2024).
- [45] L. Šmejkal, A. H. MacDonald, J. Sinova, S. Nakatsuji, and T. Jungwirth, Anomalous Hall antiferromagnets, *Nat Rev Mater* **7**, 482 (2022).
- [46] Y.-H. Wan and Q.-F. Sun, Magnetization-induced phase transitions on the surface of three-dimensional topological insulators, *Phys. Rev. B* **109**, 045418 (2024).
- [47] L. Fu and C. L. Kane, Topological insulators with inversion symmetry, *Phys. Rev. B* **76**, 045302 (2007).
- [48] P. Zhang, R. Noguchi, K. Kuroda, C. Lin, K. Kawaguchi, K. Yaji, A. Harasawa, M. Lippmaa, S. Nie, H. Weng, V. Kandyba, A. Giampietri, A. Barinov, Q. Li, G. D. Gu, S. Shin, and T. Kondo, Observation and control of the weak topological insulator state in ZrTe<sub>5</sub>, *Nat. Commun.* **12**, 406 (2021).
- [49] Y.-F. Zhou, H. Jiang, X. C. Xie, and Q.-F. Sun, Two-dimensional lattice model for the surface states of topological insulators, *Phys. Rev. B* **95**, 245137 (2017).
- [50] M. Gong, H. Liu, H. Jiang, C.-Z. Chen, and X.-C. Xie, Half-quantized helical hinge currents in axion insulators, *National Science Review* **10**, nwad025 (2023).
- [51] J.-Y. Zou, B. Fu, H.-W. Wang, Z.-A. Hu, and S.-Q. Shen, Half-quantized Hall effect and power law decay of edge-current distribution, *Phys. Rev. B* **105**, L201106 (2022).
- [52] M. Büttiker, Four-Terminal Phase-Coherent Conductance, *Phys. Rev. Lett.* **57**, 1761 (1986).
- [53] Y. Xing, Q.-f. Sun, and J. Wang, Influence of dephasing on the quantum Hall effect and the spin Hall effect, *Phys. Rev. B* **77**, 115346 (2008).
- [54] M. Buttiker, Symmetry of electrical conduction, *IBM Journal of Research and Development* **32**, 317 (1988).
- [55] W. Long, H. Zhang, and Q.-f. Sun, Quantum thermal Hall effect in graphene, *Phys. Rev. B* **84**, 075416 (2011).
- [56] C. J. Lambert, V. C. Hui, and S. J. Robinson, Multi-probe conductance formulae for mesoscopic superconductors, *J. Phys.: Condens. Matter* **5**, 4187 (1993).
- [57] H. Zhou, C.-Z. Chen, Q.-F. Sun, and X. C. Xie, Dissipative chiral channels, Ohmic scaling, and half-integer Hall conductivity from relativistic quantum Hall effect, *Phys. Rev. B* **109**, 115305 (2024).
- [58] N. Varnava and D. Vanderbilt, Surfaces of axion insulators, *Phys. Rev. B* **98**, 245117 (2018).
- [59] R. Bianco and R. Resta, Mapping topological order in coordinate space, *Phys. Rev. B* **84**, 241106 (2011).
- [60] T. Rauch, T. Olsen, D. Vanderbilt, and I. Souza, Geometric and nongeometric contributions to the surface anomalous Hall conductivity, *Physical Review B* **98**, 115108 (2018).
- [61] M. Gu, J. Li, H. Sun, Y. Zhao, C. Liu, J. Liu, H. Lu, and Q. Liu, Spectral signatures of the surface anomalous Hall effect in magnetic axion insulators, *Nat. Commun.* **12**, 3524 (2021).
- [62] J.-Y. Zou, R. Chen, B. Fu, H.-W. Wang, Z.-A. Hu, and S.-Q. Shen, Half-quantized Hall effect at the parity-invariant Fermi surface, *Phys. Rev. B* **107**, 125153 (2023).
- [63] H.-W. Wang, B. Fu, and S.-Q. Shen, Signature of parity anomaly: Crossover from one half to integer quantized Hall conductance in a finite magnetic field, *Phys. Rev. B* **109**, 075113 (2024).
- [64] T. Osumi, S. Souma, T. Aoyama, K. Yamauchi, A. Honma, K. Nakayama, T. Takahashi, K. Ohgushi, and T. Sato, Observation of a giant band splitting in altermagnetic MnTe, *Phys. Rev. B* **109**, 115102 (2024).
- [65] S. Reimers, L. Odenbreit, L. Šmejkal, V. N. Strocov, P. Constantinou, A. B. Hellenes, R. Jaeschke Ubierno, W. H. Campos, V. K. Bharadwaj, A. Chakraborty, T. Denneulin, W. Shi, R. E. Dunin-Borkowski, S. Das, M. Kläui, J. Sinova, and M. Jourdan, Direct observation of altermagnetic band splitting in CrSb thin films, *Nat. Commun.* **15**, 2116 (2024).
- [66] O. Fedchenko, J. Minár, A. Akashdeep, S. W. D'Souza, D. Vasilyev, O. Tkach, L. Odenbreit, Q. Nguyen, D. Kutnyakhov, N. Wind, L. Wenthaus, M. Scholz, K. Rossnagel, M. Hoesch, M. Aeschlimann, B. Stadtmüller, M. Kläui, G. Schönhense, T. Jungwirth, A. B. Hellenes, G. Jakob, L. Šmejkal, J. Sinova, and H.-J. Elmers, Observation of time-reversal symmetry breaking in the band structure of altermagnetic RuO<sub>2</sub>, *Sci. Adv.* **10**, eadj4883 (2024).
- [67] R. Noguchi, T. Takahashi, K. Kuroda, M. Ochi, T. Shirasawa, M. Sakano, C. Bareille, M. Nakayama, M. D. Watson, K. Yaji, A. Harasawa, H. Iwasawa, P. Dudin, T. K. Kim, M. Hoesch, V. Kandyba, A. Giampietri, A. Barinov, S. Shin, R. Arita, T. Sasagawa, and T. Kondo, A weak topological insulator state in quasi-one-dimensional bismuth iodide, *Nature* **566**, 518 (2019,2).
- [68] J. Zhong, M. Yang, Z. Shi, Y. Li, D. Mu, Y. Liu, N. Cheng, W. Zhao, W. Hao, J. Wang, L. Yang, J. Zhuang, and Y. Du, Towards layer-selective quantum spin hall channels in weak topological insulator Bi<sub>4</sub>Br<sub>2</sub>I<sub>2</sub>, *Nat. Commun.* **14**, 4964 (2023).
- [69] R. Noguchi, M. Kobayashi, K. Kawaguchi, W. Yamamori, K. Aido, C. Lin, H. Tanaka, K. Kuroda, A. Harasawa, V. Kandyba, M. Cattelan, A. Barinov, M. Hashimoto, D. Lu, M. Ochi, T. Sasagawa, and T. Kondo, Robust weak topological insulator in the bismuth halide bi<sub>4</sub>br<sub>2</sub>i<sub>2</sub>, *Phys. Rev. Lett.* **133**, 086602 (2024).